J Solid State Electrochem (2012) 16:2335–2348
DOI 10.1007/s10008-012-1703-x

ORIGINAL PAPER

Electrical, electrochemical, and thermomechanical properties of perovskite-type $(La_{1-x}Sr_x)_{1-y}Mn_{0.5}Ti_{0.5}O_{3-\delta}$ (x=0.15–0.75, y=0–0.05)

V. A. Kolotygin · E. V. Tsipis · A. I. Ivanov · Y. A. Fedotov · I. N. Burmistrov · D. A. Agarkov · V. V. Sinitsyn · S. I. Bredikhin · V. V. Kharton

Received: 24 January 2012 / Accepted: 13 February 2012 / Published online: 11 March 2012

Abstract Strontium additions in $(La_{1-x}Sr_x)_{1-y}Mn_{0.5}Ti_{0.5}O_{3-\delta}$ (x=0.15–0.75, y=0–0.05) having a rhombohedrally distorted perovskite structure under oxidizing conditions lead to the unit cell volume contraction, whilst the total conductivity, thermal and chemical expansion, and steady-state oxygen permeation limited by surface exchange increase with increasing x. The oxygen partial pressure dependencies of the conductivity and Seebeck coefficient studied at 973–1223 K in the $p(O_2)$ range from 10^{-19} to 0.5 atm suggest a dominant role of electron hole hopping and relatively stable Mn^{3+} and Ti^{4+} states. Due to low oxygen nonstoichiometry essentially constant in oxidizing and moderately reducing environments and to strong coulombic interaction between Ti^{4+} cations and oxygen anions, the tracer diffusion coefficients measured by the $^{18}O/^{16}O$ isotopic exchange depth profile method with time-of-flight secondary-ion mass spectrometric analysis are lower compared to lanthanum–strontium manganites. The average thermal expansion coefficients determined by controlled-atmosphere dilatometry vary in the range 9.8–15.0×10^{-6} K^{-1} at 300–1370 K and oxygen pressures from 10^{-21} to 0.21 atm. The anodic overpotentials of porous $La_{0.5}Sr_{0.5}Mn_{0.5}Ti_{0.5}O_{3-\delta}$ electrodes with $Ce_{0.8}Gd_{0.2}O_{2-\delta}$ interlayers, applied onto $LaGaO_3$-based solid electrolyte, are lower compared to $(La_{0.75}Sr_{0.25})_{0.95}Cr_{0.5}Mn_{0.5}O_{3-\delta}$ when no metallic current-collecting layers are introduced. However, the polarization resistance is still high, ~2 Ω×cm^2 in humidified 10 % H_2–90 % N_2 atmosphere at 1073 K, in correlation with relatively low electronic conduction and isotopic exchange rates. The presence of H_2S traces in H_2-containing gas mixtures did not result in detectable decomposition of the perovskite phases.

Keywords SOFC electrode · Electronic transport · Oxygen permeability · Chemical expansion · TOF-SIMS analysis · Controlled-atmosphere dilatometry

V. A. Kolotygin · V. V. Kharton (✉)
Department of Ceramics and Glass Engineering, CICECO,
University of Aveiro,
3810-193 Aveiro, Portugal
e-mail: kharton@ua.pt

E. V. Tsipis
Chemistry Department, Instituto Tecnológico e Nuclear,
CFMC-UL,
EN 10,
2686-953 Sacavém, Portugal

A. I. Ivanov · Y. A. Fedotov · I. N. Burmistrov · D. A. Agarkov · V. V. Sinitsyn · S. I. Bredikhin
Institute of Solid State Physics RAS, Institutskaya 2,
142432 Chernogolovka, Moscow region, Russia

Introduction

The developments of intermediate-temperature solid oxide fuel cells (SOFCs) and other electrochemical devices with solid oxide electrolytes make it necessary to search for novel electrode materials having a high electrochemical activity and a sufficient thermodynamic stability in both reducing and oxidizing atmospheres [1–5]. For the anodes of SOFCs and cathodes of solid oxide electrolysis cells (SOECs), key requirements include also a high electronic conductivity in wide ranges of the oxygen partial pressure, $p(O_2)$, catalytic activity towards target reactions such as hydrocarbon oxidation or hydrogen evolution, inertness for carbon deposition, tolerance to sulfur-containing species, thermomechanical and chemical compatibility with solid electrolyte ceramics, and low costs. The conventional Ni-containing cermets undergo degradation due to coking in hydrocarbon-fueled SOFCs and

carbon dioxide SOECs, large volume changes on redox cycling, and sulfur poisoning, all leading to operational problems. As these problems cannot be widely solved by substituting nickel with other metals, attention is drawn to oxide electrode compositions, such as perovskite-related titanates and chromites, where no metallic components are used or their amount is small [1–11]. The alternative materials known up to now exhibit, however, other functional disadvantages. For example, perovskite-related (Sr, La)$TiO_{3\pm\delta}$ and their derivatives possess substantially high electronic conductivity at low $p(O_2)$ but tend to phase transformations on oxidation and slow redox kinetics; the electrode performance of (La, Sr)$CrO_{3-\delta}$, (La, Sr)$Cr_{0.5}Mn_{0.5}O_{3-\delta}$, and their analogues suffers from rather low electronic conduction in reducing atmospheres ([4–6] and references cited therein). Another group of promising electrode materials is based on (Sr, La) (Ti, Mn)$O_{3\pm\delta}$ perovskites stable in a wide $p(O_2)$ range, which also possess relatively high electrical conductivity in air and moderate thermal and chemical expansion [1, 7–11]. The average linear thermal expansion coefficients (TECs) of $(La, Sr)_{1-y}Mn_{1-x}Ti_xO_{3-\delta}$ (x=0.4–0.6, y=0–0.05) ceramics vary in the range 11.6–14.3×10^{-6} K^{-1} at 300–1370 K, slightly increasing on reduction [1, 7, 11]. Porous $La_{0.4}Sr_{0.6}Mn_{0.6}Ti_{0.4}O_{3-\delta}$ electrodes in contact with yttria-stabilized zirconia (YSZ) solid electrolyte displayed polarization resistance of 0.8 Ω×cm^2 in 20 % H_2–3 % H_2O–Ar gas mixture at 1073 K and no carbon deposition in CH_4–3 % H_2O, although 0.6 % irreversible dimensional changes were observed on redox cycling [1, 8]. Increasing Mn content above ~50 % of the B site concentration in ABO_3 perovskite structure may have a positive effect on the electronic transport and electrochemical activity but lowers stability towards reduction down to the level inappropriate for SOFC anode applications [8]. For $La_{0.33}Sr_{0.67}Mn_{1-x}Ti_xO_{3-\delta}$, the improvement in total conductivity with decreasing x was attributed mainly to grain boundary effects [9]. The total conductivity of such materials, however, drops at low $p(O_2)$, which is critical for the anode performance and makes it necessary to incorporate electronically conducting components into the porous electrodes operating under reducing conditions [1, 4, 5, 7, 8, 11]. After infiltration of $CeO_{2-\delta}$ and Ni, the anodic overpotential of $(La_{0.25}Sr_{0.75})_{0.95}Mn_{0.5}Ti_{0.5}O_{3-\delta}$ porous layers applied onto $(La_{0.9}Sr_{0.1})_{0.98}Ga_{0.8}Mg_{0.2}O_{3-\delta}$ (LSGM) solid electrolyte with a $Ce_{0.8}Gd_{0.2}O_{2-\delta}$ (CGO) interlayer decreased down to 85 mV at 1073 K and current density of 40 mA/cm^2 [7]. For $La_{0.4}Sr_{0.6}Ti_{0.8}Mn_{0.2}O_{3-\delta}$−YSZ (50–50 wt.%) composite anodes, the addition of 10 wt.% CeO_2 and 1 wt.% Pd increased the power density of model fuel cells from 30 up to 150 mW×cm^{-2} at 1073 K [10]. The transport, electrochemical, and thermomechanical properties are essentially governed by redox couples formed by the transition metal cations in the B sublattice and should be tunable by optimizing the concentration of acceptor A-site dopant. The present work is centered on the studies of phase stability, electronic conductivity, Seebeck coefficient, ionic transport, thermal and chemical expansion, and electrochemical behavior of perovskite-type $(La_{1-x}Sr_x)_{1-y}Mn_{0.5}Ti_{0.5}O_{3-\delta}$ (x=0.15–0.75, y=0–0.05) system.

Experimental

Submicron powders of A-site-deficient $(La_{1-x}Sr_x)_{0.95}Mn_{0.5}Ti_{0.5}O_{3-\delta}$ (x=0.15–0.75) and A-site-stoichiometric $La_{0.5}Sr_{0.5}Mn_{0.5}Ti_{0.5}O_{3-\delta}$ and $La_{0.6}Sr_{0.4}Mn_{0.5}Ti_{0.5}O_{3-\delta}$ perovskites were prepared via the glycine–nitrate [7] and citrate synthesis [13] routes from high-purity $La(NO_3)_3\times 6H_2O$, $Sr(NO_3)_2$, $Mn(CH_3COO)_2\times 4H_2O$, and TiO_2. The as-synthesized products were annealed in air at 1073–1473 K with intermediate regrindings. The gas-tight ceramics (density of 94–97 %; Table 1) were sintered in air at 1623 K for 20 h or 1773 K for 10 h. The processing conditions of LSGM solid electrolyte and CGO powder, used to form protective interlayers between the working (La, Sr) (Mn, Ti)$O_{3-\delta}$ electrode and LSGM, were described in previous reports [12, 14]. Prior to the preparation of porous electrodes, intermediate CGO layers with cobalt oxide sintering aid were deposited onto the electrolyte surface followed by firing at 1473 K for 2 h, yielding the sheet density of 3 mg/cm^2. Then, the porous electrode layers (sheet density of 12–14 mg/cm^2) were applied onto the CGO interlayer and fired in air at 1473 K for 2 h. The electrode fabrication procedures and cell geometry were similar to those reported in [6]. No attempt to optimize electrode thickness and morphology was made in the present work.

The formation of single perovskite phases in dense ceramics and porous electrodes was confirmed by X-ray powder diffraction (XRD) analysis using Rigaku D/Max-B and SIEMENS D-500-Braun instruments (CuK_α radiation). Additional series of samples were annealed in reducing H_2- and H_2S-containing atmospheres to assess the phase stability under possible operating conditions. The powders, ceramic materials, and porous electrodes were characterized by scanning electron microscopy coupled with energy-dispersive spectroscopy (SEM/EDS, Hitachi S-4100/SU-70 and SUPRA 50VP instruments). The dense ceramics were also studied by controlled-atmosphere dilatometry (Linseis L75V/1250 dilatometer combined with a gas system involving an electrochemical YSZ oxygen pump and sensor), measurements of total electrical conductivity (four-probe DC) and Seebeck coefficient as a function of the oxygen partial pressure and temperature, and determination of the steady-state oxygen permeability (OP). Description of the experimental techniques and equipment used is found elsewhere ([6, 7, 12, 14] and references cited therein). For all OP data presented in this work, the oxygen partial pressure at the membrane feed side (p_2) corresponds to 0.21 atm. The dilatometric measurements were performed on heating/

Table 1 Unit cell parameters and density of as-prepared $(La_{1-x}Sr_x)_{1-y}Mn_{0.5}Ti_{0.5}O_{3-\delta}$ ceramics equilibrated at atmospheric oxygen pressure

	a, Å	*c*, Å	*V*, Å^3	ρ_{theor}, g/cm^3	ρ_{exp}/ρ_{theor}, %
$(La_{0.25}Sr_{0.75})_{0.95}Mn_{0.5}Ti_{0.5}O_{3-\delta}$	5.4960 (8)	13.455 (1)	351.97 (8)	5.52	94.0
$(La_{0.35}Sr_{0.65})_{0.95}Mn_{0.5}Ti_{0.5}O_{3-\delta}$	5.5203 (6)	13.476 (2)	355.67 (7)	5.59	91.0
$La_{0.5}Sr_{0.5}Mn_{0.5}Ti_{0.5}O_{3-\delta}$	5.530 (3)	13.515 (8)	357.96 (9)	5.88	97.4
$(La_{0.55}Sr_{0.45})_{0.95}Mn_{0.5}Ti_{0.5}O_{3-\delta}$	5.5471 (3)	13.4961 (8)	359.64 (4)	5.80	93.6
$La_{0.6}Sr_{0.4}Mn_{0.5}Ti_{0.5}O_{3-\delta}$	5.533 (2)	13.493 (3)	357.87 (6)	6.02	96.3
$(La_{0.75}Sr_{0.25})_{0.95}Mn_{0.5}Ti_{0.5}O_{3-\delta}$	5.5578 (2)	13.4996 (7)	361.13 (3)	6.05	88.3
$(La_{0.85}Sr_{0.15})_{0.95}Mn_{0.5}Ti_{0.5}O_{3-\delta}$	5.5633 (2)	13.541 (1)	362.97 (3)	6.15	92.5

a, *c*, and *V* are the unit cell parameters and volume, respectively, in hexagonal settings (space group $R\bar{3}c$);
ρ_{theor} and ρ_{exp} are the theoretical and experimental density values, respectively

cooling with a constant rate of 3 K/min and in the regime of temperature cycling in the range 923–1223 K with 50 K steps and 2–7-h dwells at each temperature as illustrated in Fig. 1. The studies of steady-state electrode polarization were carried out by the three-electrode technique in the cells with a porous Pt counter electrode (CE) symmetric to the working oxide electrode (WE), a Pt reference electrode (RE), and Pt gauze current collectors as described in [6, 7, 14]. The experiments were performed in galvanostatic mode using a PGSTAT302 Autolab instrument at 873–1073 K, exposing WE and RE to flowing 10 % H_2–N_2 gas mixture humidified at room temperature; atmospheric air was supplied over the counter electrode. After electrochemical tests, the half-cells were again examined by XRD and SEM/EDS in order to reveal possible changes in the phase composition and microstructure.

The bulk oxygen tracer diffusion (*D**) and surface exchange (*k*) coefficients were assessed using the $^{18}O/^{16}O$ isotopic exchange depth profile method as described in [15]. Prior to $^{18}O/^{16}O$ exchange annealing, the polished

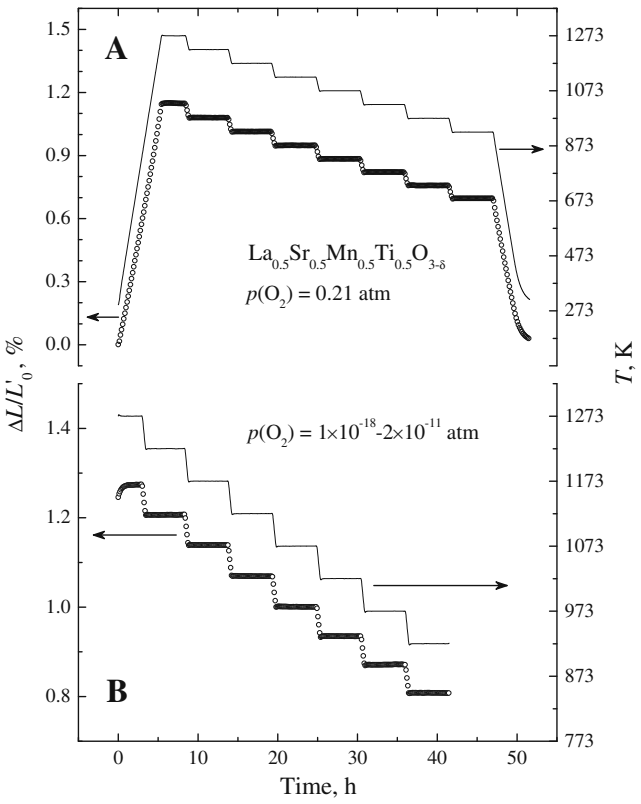

Fig. 1 Illustration of the regimes used for the controlled-atmosphere dilatometric measurements in flowing air (**a**) and CO–CO_2 gas mixtures (**b**) on temperature cycling at 923–1223 K with equilibration at each temperature, for $La_{0.5}Sr_{0.5}Mn_{0.5}Ti_{0.5}O_{3-\delta}$ ceramics. L'_0 is the initial length at room temperature in air

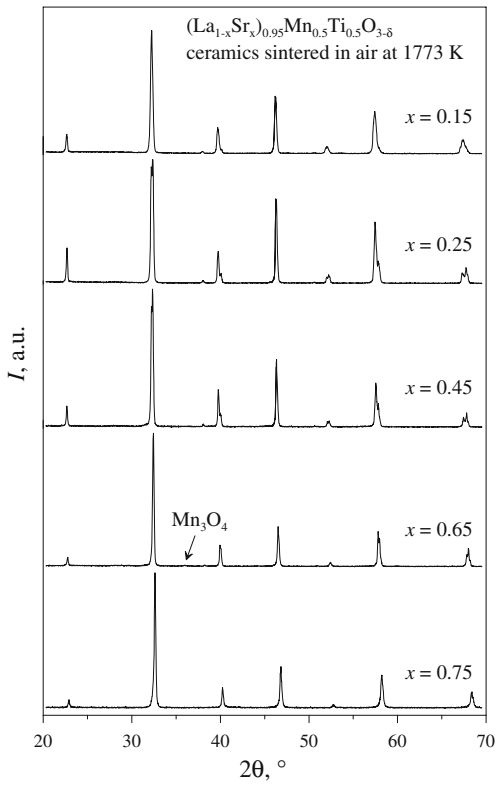

Fig. 2 XRD patterns of $(La_{1-x}Sr_x)_{0.95}Mn_{0.5}Ti_{0.5}O_{3-\delta}$ after sintering in air at 1773 K and slow cooling

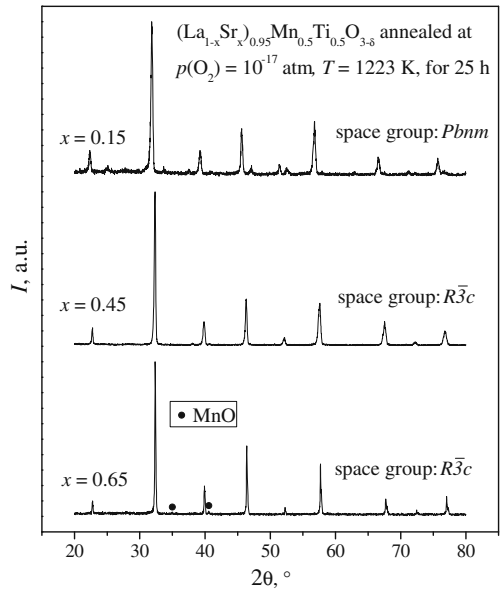

Fig. 3 Examples of XRD patterns of $(La_{1-x}Sr_x)_{0.95}Mn_{0.5}Ti_{0.5}O_{3-\delta}$ after reduction in flowing H_2–H_2O–N_2 gas mixture with $p(O_2) \approx 10^{-17}$ atm at 1223 K during 25 h

and cleaned ceramic samples were equilibrated in air of normal isotopic abundance; then, the chamber was evacuated and labeled oxygen (95 % enriched $^{18}O_2$) was introduced to reach $p(O_2)$=0.2 atm. The samples were annealed at 1023–1223 K for a required time (1–45.5 h) and then quenched. The ^{18}O penetration profiles were determined by time-of-flight secondary-ion mass spectrometry (TOF-SIMS) using a TOF-SIMS.5-100P instrument (ION-TOF GmbH, Germany) operated in the depth profile mode, with a 45° incidence 25 keV Bi^+ primary ion beam and 45° incidence 2 keV Cs^+ sputter ion beam. The crater depth was measured after the SIMS analysis by surface profilometry (Taylor–Hobson Talystep). The rate of isotopic exchange across the gas/solid interface is assumed to be directly proportional to the difference in isotope concentration (C) between the gas and the solid, leading to the boundary condition [16–18]:

$$-D^* \left.\frac{\partial C}{\partial x}\right|_{x=0} = k\left(C_g - C_s\right) \tag{1}$$

where x is the depth and C_g and C_s are the ^{18}O isotope ratio in the gas phase and in the surface, respectively. Assuming that the isotope concentration in the gas phase is constant, the diffusion equation for this boundary condition and a semi-infinite medium is formulated as [16–18]:

$$\frac{C(x,t) - C_{bg}}{C_g - C_{bg}} = \operatorname{erfc}\left(\frac{x}{2\sqrt{D^* t}}\right) - \exp\left(\frac{kx + k^2 t}{D^*}\right) \times \operatorname{erfc}\left(\frac{x + 2kt}{2\sqrt{D^* t}}\right) \tag{2}$$

where $C(x, t)$ is the ^{18}O isotope fraction, t is the exchange annealing time, and C_{bg} is the natural background level of ^{18}O (0.20 %). D^* and k were obtained by non-linear least squares fitting of the SIMS data to Eq. 2.

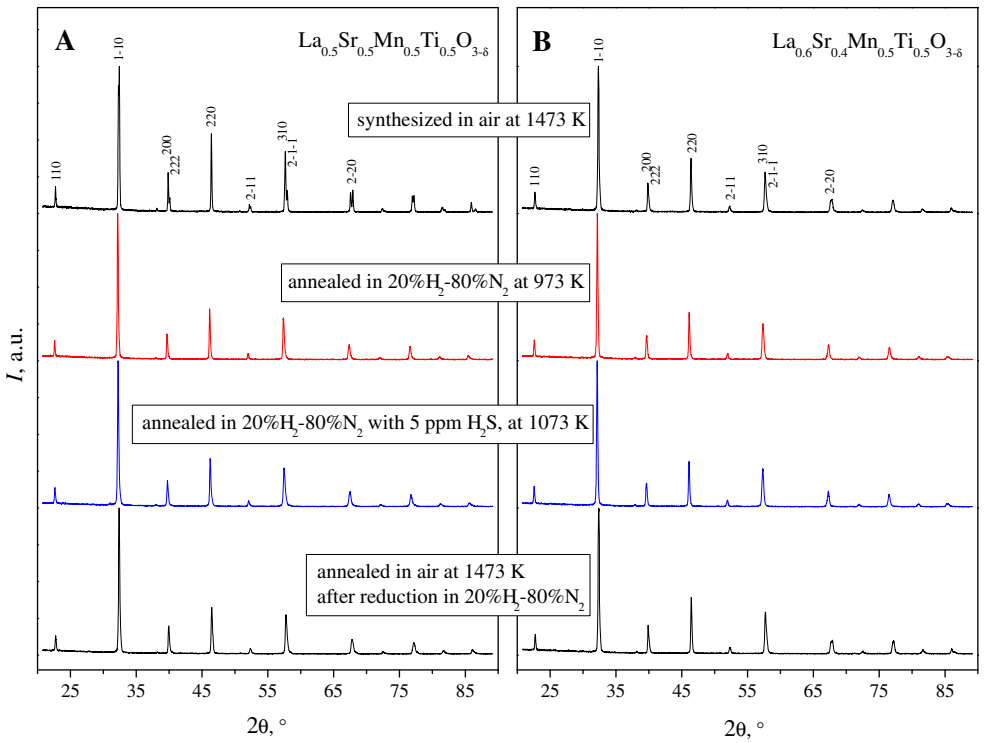

Fig. 4 Selected XRD patterns of $La_{0.5}Sr_{0.5}Mn_{0.5}Ti_{0.5}O_{3-\delta}$ (**a**) and $La_{0.6}Sr_{0.4}Mn_{0.5}Ti_{0.5}O_{3-\delta}$ (**b**) after preparation, after annealing in H_2- and H_2S-containing atmospheres, and after subsequent annealing in air. Conditions of the thermal treatments are given in the legends

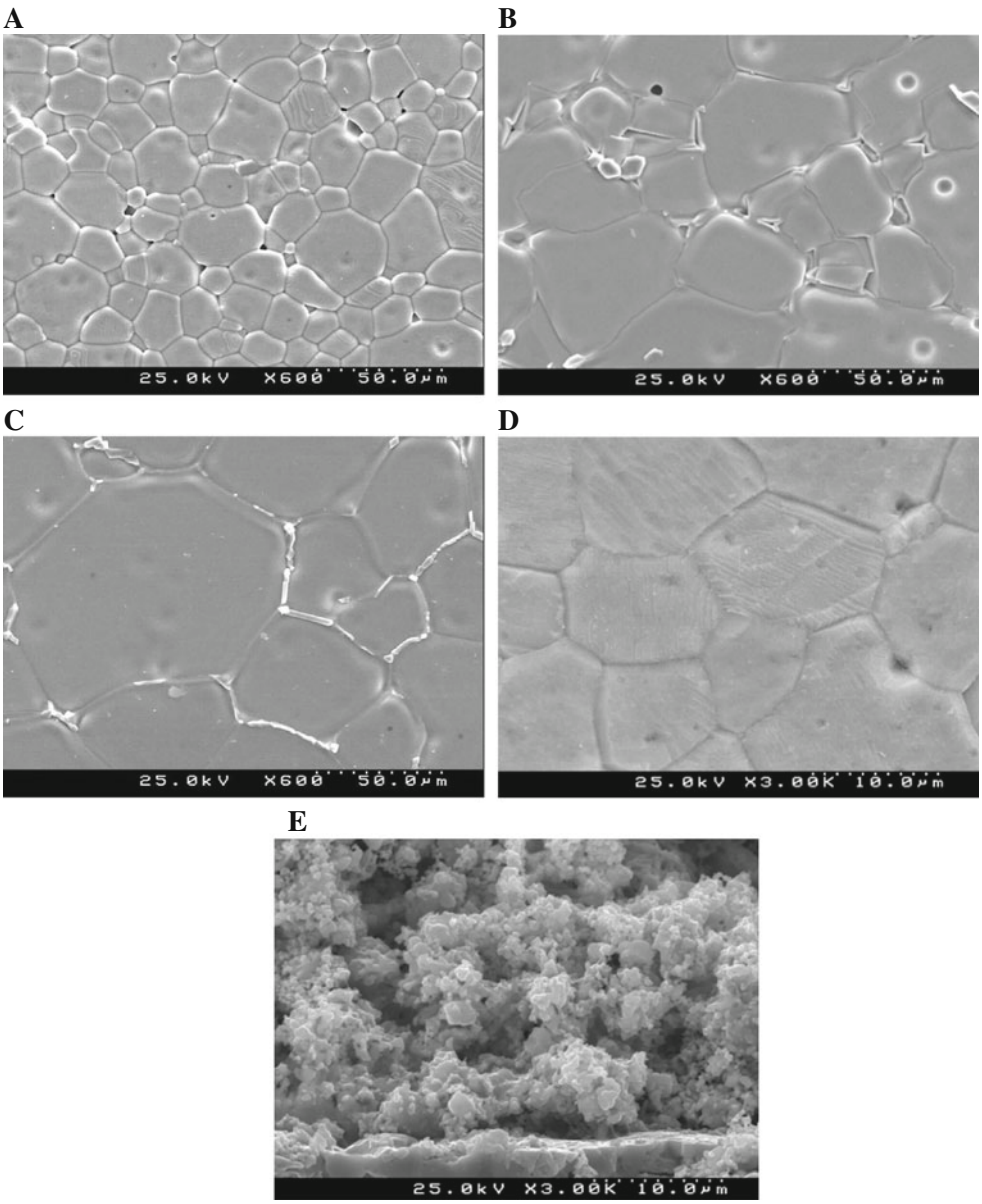

Fig. 5 SEM micrographs of $(La_{0.35}Sr_{0.65})_{0.95}Mn_{0.5}Ti_{0.5}O_{3-\delta}$ (**a**), $(La_{0.55}Sr_{0.45})_{0.95}Mn_{0.5}Ti_{0.5}O_{3-\delta}$ (**b**), $(La_{0.75}Sr_{0.25})_{0.95}Mn_{0.5}Ti_{0.5}O_{3-\delta}$ (**c**), and $(La_{0.85}Sr_{0.15})_{0.95}Mn_{0.5}Ti_{0.5}O_{3-\delta}$ (**d**) sintered in air at 1773 K, polished, and thermally etched, and a fractured half-cell with porous $La_{0.5}Sr_{0.5}Mn_{0.5}Ti_{0.5}O_{3-\delta}$ electrode and LSGM solid electrolyte after electrochemical measurements (**e**)

Results and discussion

Phase composition and crystal structure

XRD analysis showed that all synthesized perovskites listed in Table 1, namely, $La_{1-x}Sr_xMn_{0.5}Ti_{0.5}O_{3-\delta}$ (x=0.4–0.5) and $(La_{1-x}Sr_x)_{0.95}Mn_{0.5}Ti_{0.5}O_{3-\delta}$ (x=0.15–0.75), are single phase. The only exception relates to $(La_{0.35}Sr_{0.65})_{0.95}Mn_{0.5}Ti_{0.5}O_{3-\delta}$ where one peak of Mn_3O_4, comparable to the background, might be suspected in the XRD pattern (Fig. 2). After equilibration with atmospheric oxygen, the crystal structure was refined as rhombohedrally distorted perovskite (space group $R\bar{3}c$). Table 1 lists the lattice parameters presented in hexagonal settings. In general, the unit cell volume of cation-deficient perovskites tends to decrease with increasing x, on the contrary to the average cation radius variations in the A-sublattice [19]. An analogous trend is known for $La_{1-x}Sr_xMnO_{3\pm\delta}$ system (e.g., [20]) where Sr^{2+} doping is charge-compensated by the Mn^{4+} formation and, for moderate strontium additions when no significant oxygen deficiency appears, the Curie temperature increases with x. Most likely, the situation in oxidized $(La_{1-x}Sr_x)_{0.95}Mn_{0.5}Ti_{0.5}O_3$ is similar, suggesting that the average oxidation state of manganese cations should increase when x increases, which is in general agreement with the conductivity variations. The creation of A-site cation vacancies leads to the unit cell volume expansion (Table 1), a result of stronger coulombic repulsion between the oxygen anions [21]. This factor also seems relevant for the La-rich compositions, where the crystal electroneutrality and

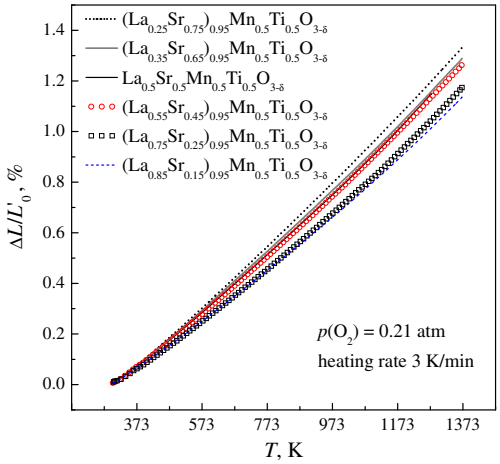

Fig. 6 Dilatometric curves of $(La_{1-x}Sr_x)_{1-y}Mn_{0.5}Ti_{0.5}O_{3-\delta}$ ceramics in air collected on continuous heating (3 K min^{-1}). L'_0 is the initial length at room temperature in air

lattice conservation conditions may lead to the formation of extra cation vacancies instead of Mn^{2+}.

No perovskite phase decomposition was observed on reduction in H_2–H_2O–N_2 atmospheres (Figs. 3 and 4). The traces of MnO observed in the XRD pattern of $(La_{0.35}Sr_{0.65})_{0.95}Mn_{0.5}Ti_{0.5}O_{3-\delta}$ (Fig. 3) originate from Mn_3O_4 reduction. The lattice volume of reduced $(La_{1-x}Sr_x)_{1-y}Mn_{0.5}Ti_{0.5}O_{3-\delta}$ expands by 1–2 % with respect to the oxidized phases at room temperature due to lowering oxidation state of the B-site cations, increasing their average radii, and the oxygen vacancy formation promoting cation repulsion. In cases when the structure transforms from rhombohedral to orthorhombic, larger volume variations are observed. Notice that even

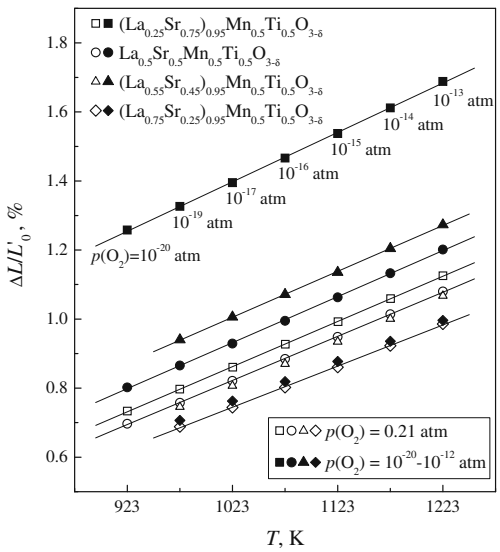

Fig. 7 Selected dilatometric data on $(La_{1-x}Sr_x)_{1-y}Mn_{0.5}Ti_{0.5}O_{3-\delta}$ ceramics, collected in the regime of isothermal dwells for equilibration at each temperature in air and CO–CO_2. The $p(O_2)$ values in the CO–CO_2 atmosphere are marked for $(La_{0.25}Sr_{0.75})_{0.95}Mn_{0.5}Ti_{0.5}O_{3-\delta}$

cation-stoichiometric $La_{1-x}Sr_xMn_{0.5}Ti_{0.5}O_{3-\delta}$ (x=0.4–0.5) remain single phase after annealing in a 20 % H_2–80 % N_2 flow containing 5 ppm H_2S during 12–24 h at 973–1073 K (Fig. 4). This behavior being reproducible for various compositions indicates a good stability of reduced (La, Sr) $Mn_{0.5}Ti_{0.5}O_{3-\delta}$ in fuel gases, although possible sulfur-poisoning surface effects on the electrocatalytic activity require careful investigations. Another necessary comment is that, in most cases, reduction at 973–1223 K did not cause the rhombohedral → orthorhombic transition, except for the compositions with low strontium concentration (x=0.15–0.25). Reductive annealing at temperatures above 1273 K, either in H_2-containing atmospheres or in vacuum, promotes this transformation.

Microstructural characterization

Typical microstructures of $(La_{1-x}Sr_x)_{1-y}Mn_{0.5}Ti_{0.5}O_{3-\delta}$ dense ceramics and porous electrodes are illustrated in Fig. 5. SEM inspection of the ceramic materials showed modest traces of glassy phases at the grain boundaries (e.g., see Fig. 5b, c), suggesting a liquid phase-assisted sintering process. At the same time, no significant compositional inhomogeneities were revealed by EDS within the limits of experimental uncertainty. The largest grain size, up to ~100 μm, was found for the ceramics with intermediate strontium concentrations, x=0.25–0.45. The electrode layers exhibit homogeneous porous microstructures where submicron grain size is preserved (Fig. 5e). No essential microstructural changes were observed after electrochemical testing.

Thermal and chemical expansion

Selected results of the controlled-atmosphere dilatometric measurements performed in the regimes of continuous heating and isothermal dwells with equilibration at 923–1223 K are presented in Figs. 6 and 7, respectively. Tables 2 and 3 summarize the average thermal expansion coefficients in air, argon, and CO–CO_2 atmospheres and the values of reduction-induced strains. As for the other titanate- and manganite-based materials [1, 6–8, 11], the apparent TECs vary in the range 9.8–15.0×10^{-6} K^{-1}, slightly increasing on heating due to oxygen losses from the lattice (Fig. 6; Table 2). Increasing strontium content in $(La_{1-x}Sr_x)_{1-y}Mn_{0.5}Ti_{0.5}O_{3-\delta}$, charge-compensated by increasing oxidation states of manganese cations, results in larger oxygen nonstoichiometry variations on heating and on reduction. These variations are reflected by higher values of the apparent TECs under similar conditions (Table 2) and by larger chemical expansion (Fig. 7; Table 3). The TECs are essentially unaffected by the oxygen partial pressure variations in oxidizing environments and tend to moderately increase in reducing atmospheres, again

Table 2 Average linear thermal expansion coefficients of $(La_{1-x}Sr_x)_{1-y}Mn_{0.5}Ti_{0.5}O_{3-\delta}$ ceramics

Composition	Measuring regime	$p(O_2)$, atm	T, K	TEC×10^6, K^{-1}
$(La_{0.25}Sr_{0.75})_{0.95}Mn_{0.5}Ti_{0.5}O_{3-\delta}$	Heating, 3 K/min	0.21	1223–1373	14.0±0.1
			923–1223	13.1±0.1
			303–923	11.8±0.1
	Isothermal dwells (50 K steps)	6×10^{-4}	973–1223	13.3±0.2
		5×10^{-21}–3×10^{-13}	923–1223	14.3±0.1
$(La_{0.35}Sr_{0.65})_{0.95}Mn_{0.5}Ti_{0.5}O_{3-\delta}$	Heating, 3 K/min	0.21	1223–1373	13.5±0.1
			923–1223	12.4±0.1
			303–923	11.4±0.1
$La_{0.5}Sr_{0.5}Mn_{0.5}Ti_{0.5}O_{3-\delta}$	Cooling, 3 K/min	0.21	1073–1273	13.2±0.1
			473–1073	11.7±0.1
		1×10^{-4}	1073–1273	13.2±0.1
			473–1073	12.0±0.1
		1×10^{-15}–2×10^{-11}	1073–1273	13.7±0.1
			473–1073	12.2±0.1
	Isothermal dwells	0.21	923–1273	12.8±0.1
		1×10^{-4}	923–1273	12.9±0.1
		3×10^{-20}–2×10^{-11}	923–1273	13.4±0.2
$(La_{0.55}Sr_{0.45})_{0.95}Mn_{0.5}Ti_{0.5}O_{3-\delta}$	Heating, 3 K/min	0.21	1223–1373	13.4±0.1
			923–1223	12.5±0.1
			303–923	11.0±0.1
	Isothermal dwells	9×10^{-5}	973–1223	12.5±0.2
		3×10^{-18}–4×10^{-12}	973–1223	13.3±0.3
$(La_{0.75}Sr_{0.25})_{0.97}Mn_{0.5}Ti_{0.5}O_{3-\delta}$	Heating, 3 K/min	0.21	1073–1273	15.0±0.2
			473–1073	11.4±0.1
	Cooling, 3 K/min	1×10^{-15}–2×10^{-11}	1073–1273	12.5±0.1
			473–1073	10.8±0.1
$(La_{0.75}Sr_{0.25})_{0.95}Mn_{0.5}Ti_{0.5}O_{3-\delta}$	Heating, 3 K/min	0.21	1223–1373	13.1±0.1
			923–1223	11.4±0.1
			303–923	10.0±0.1
	Isothermal dwells	9×10^{-5}	973–1223	11.8±0.3
		3×10^{-18}–4×10^{-12}	973–1223	11.6±0.2
$(La_{0.85}Sr_{0.15})_{0.95}Mn_{0.5}Ti_{0.5}O_{3-\delta}$	Heating, 3 K/min	0.21	1223–1373	12.4±0.1
			923–1223	11.1±0.1
			303–923	9.8±0.1
	Isothermal dwells	9×10^{-5}	973–1223	11.4±0.3
		3×10^{-18}–4×10^{-12}	973–1223	11.8±0.3

correlating with the chemically induced strains and conductivity variations discussed below. Note that the isothermal lattice expansion on reduction occurs due to lowering average oxidation state and increasing radius of the transition metal cations; the former factor is related to the concentration of electronic charge carriers, determining electronic conductivity and Seebeck coefficient (α). In accordance with the XRD results, the chemically induced expansion is lower than 0.03 % under oxidizing conditions and achieves almost 0.6 % when $p(O_2)$ is reduced from 0.21 atm down to 10^{-18}–10^{-12} atm (Table 3). Nonetheless, it should be separately stressed that the overall level of thermal- and chemical-induced strains, observed in the wide range of temperature and oxygen partial pressure, is still moderate; the title materials are thermomechanically compatible with various solid oxide electrolytes, such as stabilized zirconia, CGO, or LSGM ([12, 22] and references cited therein). For the composition with maximum expansion studied in this work, $(La_{0.25}Sr_{0.75})_{0.95}Mn_{0.5}Ti_{0.5}O_{3-\delta}$, the compatibility issues were quantitatively analyzed in the previous report [7], whereas increasing lanthanum concentration leads to lower strains.

Table 3 Relative isothermal elongation of $(La_{1-x}Sr_x)_{1-y}Mn_{0.5}Ti_{0.5}O_{3-\delta}$ ceramics on reduction with respect to the length in air (L_0)

Composition	T, K	Air → Ar		Air → CO–CO_2	
		$p(O_2)$, atm	$\Delta L/L_0$, %	$p(O_2)$, atm	$\Delta L/L_0$, %
$(La_{0.25}Sr_{0.75})_{0.95}Mn_{0.5}Ti_{0.5}O_{3-\delta}$	1223	6×10^{-4}	0.0250	3×10^{-13}	0.556
	1173		0.0207	3×10^{-14}	0.546
	1023		0.0204	2×10^{-15}	0.539
	1073		0.0219	1×10^{-16}	0.534
	1023		0.0214	6×10^{-18}	0.530
	973		0.0196	2×10^{-19}	0.525
$La_{0.5}Sr_{0.5}Mn_{0.5}Ti_{0.5}O_{3-\delta}$	1223	1×10^{-4}	0.0016	2×10^{-12}	0.120
	1173		0.0021	2×10^{-13}	0.118
	1023		0.0017	2×10^{-14}	0.114
	1073		0.0011	1×10^{-15}	0.109
	1023		0.0001	5×10^{-17}	0.107
	973		0.0007	2×10^{-18}	0.107
$(La_{0.55}Sr_{0.45})_{0.95}Mn_{0.5}Ti_{0.5}O_{3-\delta}$	1223		–	4×10^{-12}	0.204
	1173			4×10^{-13}	0.202
	1023			3×10^{-14}	0.199
	1073			2×10^{-15}	0.199
	1023			8×10^{-17}	0.198
	973			3×10^{-18}	0.192
$(La_{0.75}Sr_{0.25})_{0.95}Mn_{0.5}Ti_{0.5}O_{3-\delta}$	1223		–	4×10^{-12}	0.010
	1173			4×10^{-13}	0.012
	1023			3×10^{-14}	0.016
	1073			2×10^{-15}	0.016
	1023			8×10^{-17}	0.018
	973			3×10^{-18}	0.018

L_0 is the length at the same temperature and atmospheric oxygen pressure

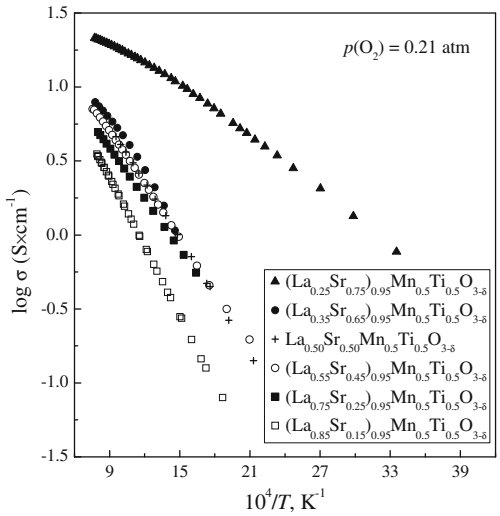

Fig. 8 Temperature dependencies of the total conductivity of $(La_{1-x}Sr_x)_{1-y}Mn_{0.5}Ti_{0.5}O_{3-\delta}$ ceramics in air

Electronic transport

The temperature dependencies of total conductivity (σ) of $(La_{1-x}Sr_x)_{1-y}Mn_{0.5}Ti_{0.5}O_{3-\delta}$ in air are presented in Fig. 8. The conductivity is predominantly electronic as shown by the oxygen permeation and diffusivity data presented below and has a thermally activated character. For the compositions with x = 0.15–0.65, the activation energies (E_a) are quite similar, varying in the narrow range 29–37 kJ/mol at 473–1283 K (Table 4). In general, acceptor-type doping increases the electronic transport, suggesting that the p-type charge carriers are prevailing under oxidizing conditions. The conductivity values of $(La_{0.25}Sr_{0.75})_{0.95}Mn_{0.5}Ti_{0.5}O_{3-\delta}$ are however substantially higher than for the other materials, whilst the E_a is lower, 15–16 kJ/mol. As mentioned in the previous report [7], such difference in behavior may indicate a tendency to the transition from small-polaron hopping to broad-band conduction mechanism, caused by rising Mn^{4+} concentration and accompanied with lowering activation energy for the electronic charge carrier mobility. These

Table 4 Activation energies for the total electrical conductivity in air, steady-state oxygen permeation fluxes through dense ceramic membranes (the permeation fluxes correspond to the oxygen pressure gradient of 0.209/0.021 atm and the membrane thickness of 1.00 mm) and oxygen tracer diffusion coefficients (the exchange annealing was performed at p ($^{18}O_2$)=0.2 atm)

Composition	Total conductivity		Oxygen permeability		Diffusion coefficient	
	T, K	E_a, kJ/mol	T, K	E_a, kJ/mol	T, K	E_a, kJ/mol
$(La_{0.25}Sr_{0.75})_{0.95}Mn_{0.5}Ti_{0.5}O_{3-\delta}$	553–873	15.6±0.1	1223–1248	169		
	943–1263	16.1±0.1				
$(La_{0.35}Sr_{0.65})_{0.95}Mn_{0.5}Ti_{0.5}O_{3-\delta}$	733–1283	30±1	1198–1273	229		
$La_{0.5}Sr_{0.5}Mn_{0.5}Ti_{0.5}O_{3-\delta}$	473–1053	30.3±0.2			1073–1223	234
$(La_{0.55}Sr_{0.45})_{0.95}Mn_{0.5}Ti_{0.5}O_{3-\delta}$	573–1263	30.1±0.2				
$La_{0.6}Sr_{0.4}Mn_{0.5}Ti_{0.5}O_{3-\delta}$					1123–1223	299
$(La_{0.75}Sr_{0.25})_{0.95}Mn_{0.5}Ti_{0.5}O_{3-\delta}$	603–1253	28.9±0.4				
$(La_{0.85}Sr_{0.15})_{0.95}Mn_{0.5}Ti_{0.5}O_{3-\delta}$	533–1263	36.5±0.4	1223–1273	170		

mechanisms are known for $LaMnO_3$-based solid solutions and for doped $SrTiO_{3-\delta}$ and $SrMnO_{3-\delta}$, respectively [23–25], although the absolute values of the Seebeck coefficient of $(La_{0.25}Sr_{0.75})_{0.95}Mn_{0.5}Ti_{0.5}O_{3-\delta}$ (Figs. 9 and 10) cannot provide a supporting evidence for such hypothesis. Whatever the microscopic mechanisms, the electrical properties of (La, Sr)$Mn_{0.5}Ti_{0.5}O_{3-\delta}$ perovskites are essentially independent of the oxygen chemical potential in oxidizing and moderately reducing atmospheres (Figs. 9, 10, and 11), thus indicating that the oxygen stoichiometry changes in these conditions are very minor. Further reduction induces oxygen deficiency, which results in higher Seebeck coefficient and lower conductivity. This behavior observed for all compositions gives another argument in favor of dominating p-type electronic transport. The variations of the conductivity and thermopower are accompanied with strong hystereses on redox cycling (Fig. 12), with an apparently irreversible behavior for the La-rich materials. The irreversibility was attributed mainly to the microcrack

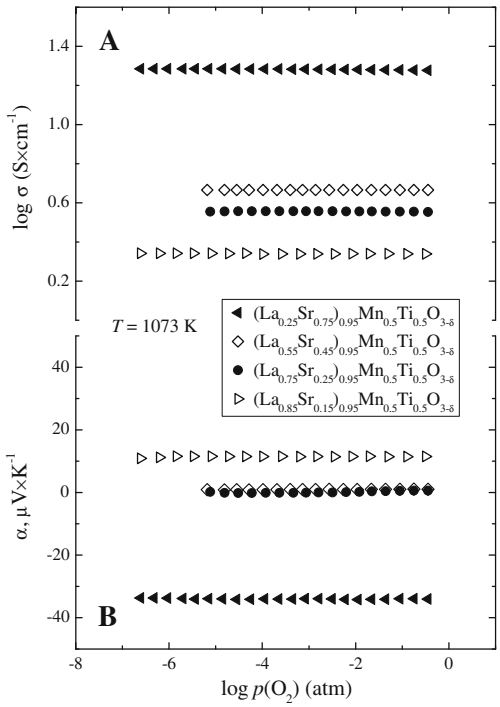

Fig. 9 Oxygen partial pressure dependencies of the total conductivity (**a**) and Seebeck coefficient (**b**) of $(La_{1-x}Sr_x)_{0.95}Mn_{0.5}Ti_{0.5}O_{3-\delta}$ under oxidizing conditions at 1073 K

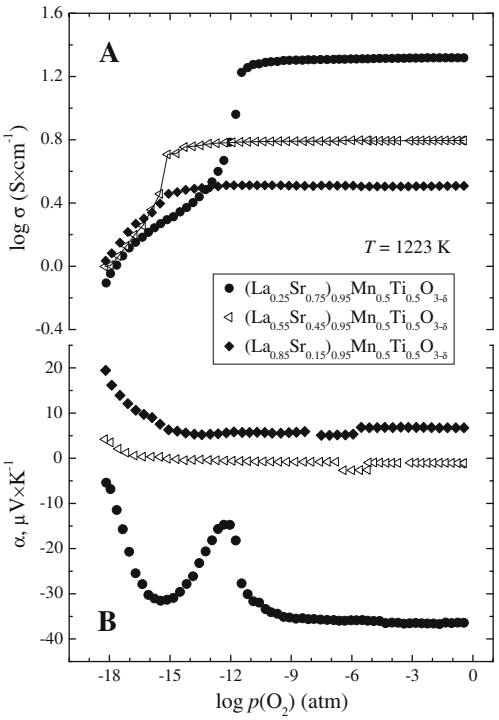

Fig. 10 Oxygen partial pressure dependencies of the total conductivity (**a**) and Seebeck coefficient (**b**) of selected $(La_{1-x}Sr_x)_{0.95}Mn_{0.5}Ti_{0.5}O_{3-\delta}$ compositions at 1223 K

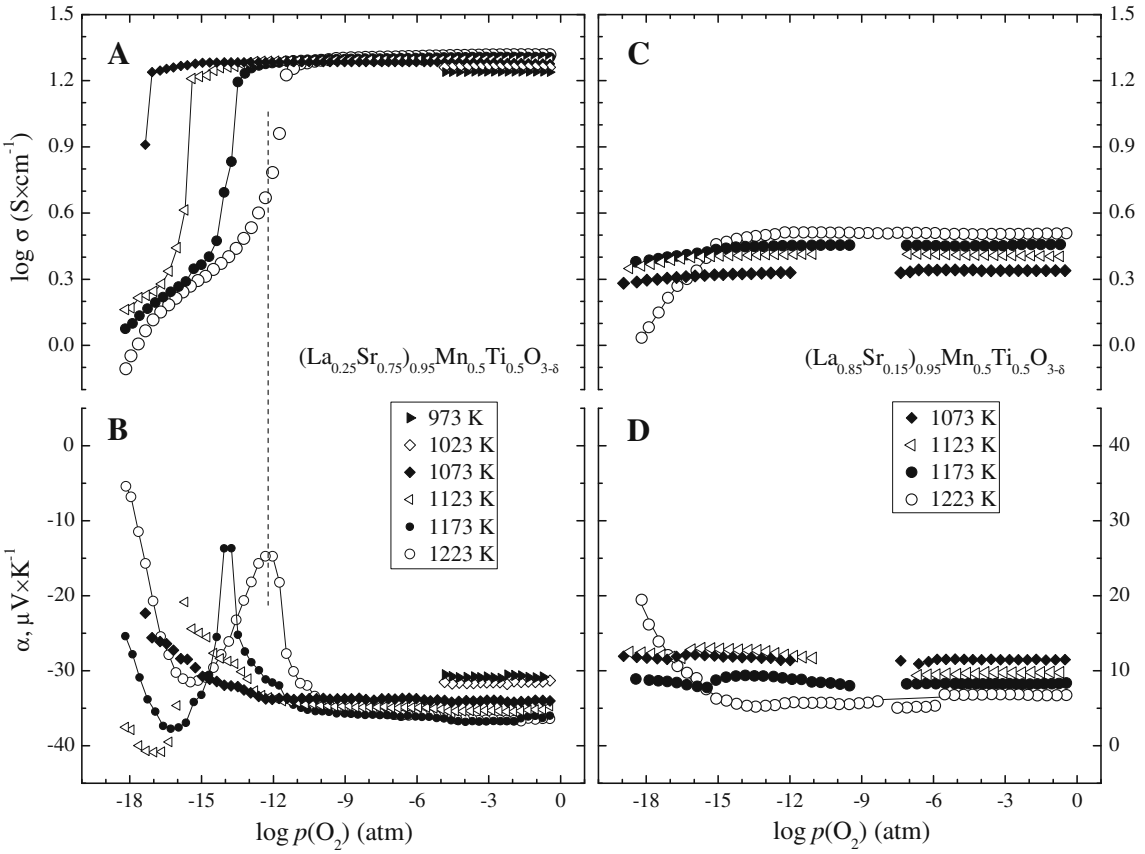

Fig. 11 Oxygen partial pressure dependencies of the total conductivity (**a**, **c**) and Seebeck coefficient (**b**, **d**) of $(La_{0.25}Sr_{0.75})_{0.95}Mn_{0.5}Ti_{0.5}O_{3-\delta}$ (**a**, **b**) and $(La_{0.85}Sr_{0.15})_{0.95}Mn_{0.5}Ti_{0.5}O_{3-\delta}$ (**c**, **d**) at 973–1223 K

formation detected by SEM and optical microscopy inspections; however, kinetics of the "orthorhombic ↔ rhombohedral" transition revealed by XRD (Figs. 2 and 3) and defect reactions involving Ti^{4+}/Ti^{3+} redox couple may also be relevant in the present case. The latter reactions are often responsible for an apparently irreversible behavior observed in perovskite-like titanates on redox cycling (e.g., [26]).

Another important feature is that increasing x in $(La_{1-x}Sr_x)_{1-y}Mn_{0.5}Ti_{0.5}O_{3-\delta}$ lowers the thermopower down to negative values. For moderate doping levels, when the average oxidation state of manganese cations is close to 3+, the Seebeck coefficient is almost 0 (Figs. 9 and 10). If the interaction between $Mn^{3+/4+}$, $Mn^{3+/2+}$, and $Ti^{4+/3+}$ states is strong enough and one type of the electronic charge carriers prevails, the latter situation may take place when the charge carrier concentration corresponds to approximately half of the density of states. In such case, increasing the fraction of Mn^{4+} compensating large Sr^{2+} additions leads to the hole concentration above 50 % sites available for their location, shifting the Seebeck coefficient down to negative values; increasing La^{3+} concentration has an opposite effect. From a theoretical point of view, an ideal situation in this case could be expected for parent stoichiometric $La^{3+}_{0.5}Sr^{2+}_{0.5}Mn^{3+}_{0.5}Ti^{4+}_{0.5}O_3$ where the level of thermopower should be primarily determined by the parameters independent of the charge carrier concentration, such as transported heat. For the related compositions with similar La^{3+} and Sr^{2+} concentrations, an analogous behavior may appear if the deviations from ideal [La]/[Sr]=1 ratio are charge-compensated by ionic point defects, namely, cation or oxygen vacancies, as for (La, Sr)$MnO_{3\pm\delta}$ with modest strontium content [27–29]. Such assumptions may explain the fact that the nearly zero thermopower values are observed for the compositions with intermediate Sr^{2+} concentrations, particularly for $(La_{0.55}Sr_{0.45})_{0.95}Mn_{0.5}Ti_{0.5}O_{3\pm\delta}$ and $(La_{0.75}Sr_{0.25})_{0.95}Mn_{0.5}Ti_{0.5}O_{3\pm\delta}$ (Fig. 9), where the oxygen nonstoichiometry expected for the predominant trivalent state of manganese cations is lower than 0.05–0.06 anions per formula unit. In the case of charge compensation via the cation vacancy formation, this level of nonstoichiometry may still be tolerated by the perovskite lattice. The electronic conductivity of these materials increases with x but exhibits quite similar values (Figs. 8 and 9) in contrast to $(La_{0.25}Sr_{0.75})_{0.95}Mn_{0.5}Ti_{0.5}O_{3-\delta}$ and $(La_{0.85}Sr_{0.15})_{0.95}Mn_{0.5}Ti_{0.5}O_{3\pm\delta}$. Finally, one should mention that the experimentally observed trends cannot completely exclude more complex mechanisms when several types of the electronic charge carriers may be present and low absolute values of the Seebeck coefficient correspond to comparable contributions of the p- and n-type charge carriers, i.e. $t_p\alpha_p \approx t_n\alpha_n$ where t is the transference number. However, no

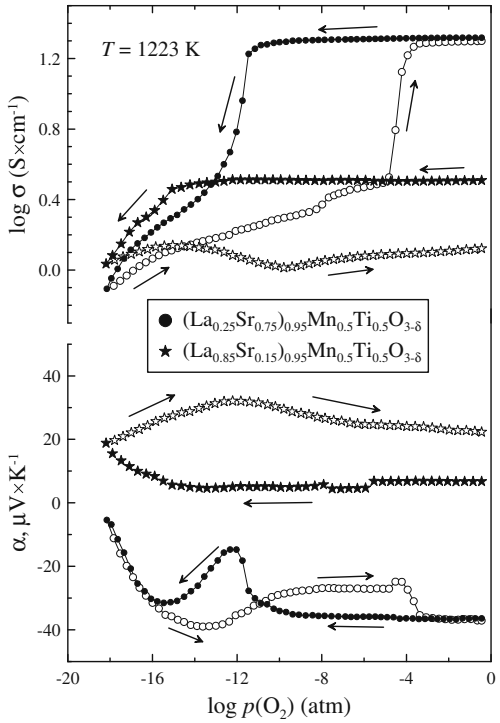

Fig. 12 Examples of the total conductivity and Seebeck coefficient variations of $(La_{0.25}Sr_{0.75})_{0.95}Mn_{0.5}Ti_{0.5}O_{3-\delta}$ and $(La_{0.85}Sr_{0.15})_{0.95}Mn_{0.5}Ti_{0.5}O_{3-\delta}$ on $p(O_2)$ cycling at 1223 K, showing strong hystereses on reoxidation (see text)

indication of significant n-type contribution can be identified from the conductivity dependencies on oxygen partial pressure and cation composition.

Oxygen permeation and diffusion

In order to evaluate the factors influencing ionic transport in $(La_{1-x}Sr_x)_{1-y}Mn_{0.5}Ti_{0.5}O_{3-\delta}$ perovskites, the steady-state oxygen permeation fluxes through dense membranes with

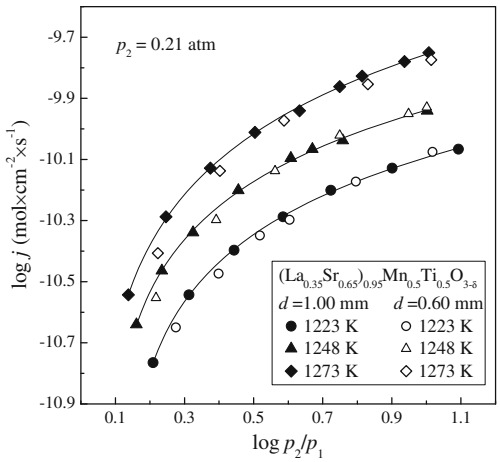

Fig. 13 Steady-state oxygen permeation fluxes through the dense $(La_{0.35}Sr_{0.65})_{0.95}Mn_{0.5}Ti_{0.5}O_{3-\delta}$ membranes with various thicknesses. The feed-side oxygen pressure (p_2) corresponds to 0.21 atm

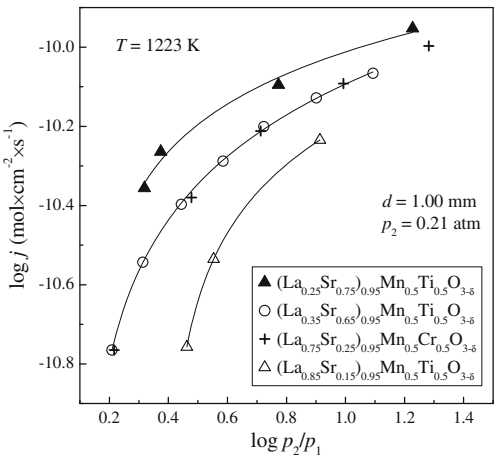

Fig. 14 Oxygen permeation fluxes through dense $(La_{1-x}Sr_x)_{0.95}Mn_{0.5}Ti_{0.5}O_{3-\delta}$ ceramic membranes at 1223 K. The membrane thickness is 1.00±0.02 mm

various thicknesses (d) were measured. The experiments demonstrated, however, a dominant limiting effect of the oxygen surface exchange kinetics; any estimation of the bulk ionic conductivity was impossible. A similar behavior was earlier observed for dense $(La_{1-x}Sr_x)_{1-y}MnO_{3-\delta}$ ceramics with x=0.4–0.6 [30]. For example, Fig. 13 displays the data on oxygen permeation fluxes (j) through $(La_{0.35}Sr_{0.65})_{0.95}Mn_{0.5}Ti_{0.5}O_{3-\delta}$ membranes as a function of the oxygen partial pressure gradient expressed via the (p_2/p_1) ratio, where p_1 and p_2 are the oxygen pressures at the membrane permeate and feed sides, respectively. The oxygen fluxes are essentially equal for the 0.60- and 1.00-mm-thick ceramics within the limits of experimental error. This tendency unambiguously indicates that oxygen transport is governed by the surface exchange rate, on the contrary to

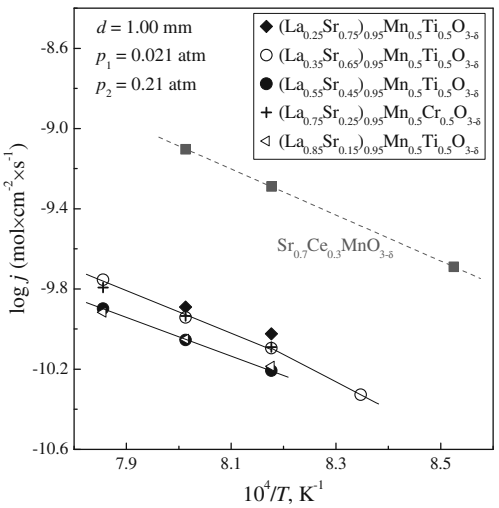

Fig. 15 Temperature dependencies of the oxygen permeation fluxes through dense $(La_{1-x}Sr_x)_{0.95}Mn_{0.5}Ti_{0.5}O_{3-\delta}$ membranes under a fixed $p(O_2)$ gradient. The data on $Sr_{0.7}Ce_{0.3}MnO_{3-\delta}$ [25] are shown for comparison

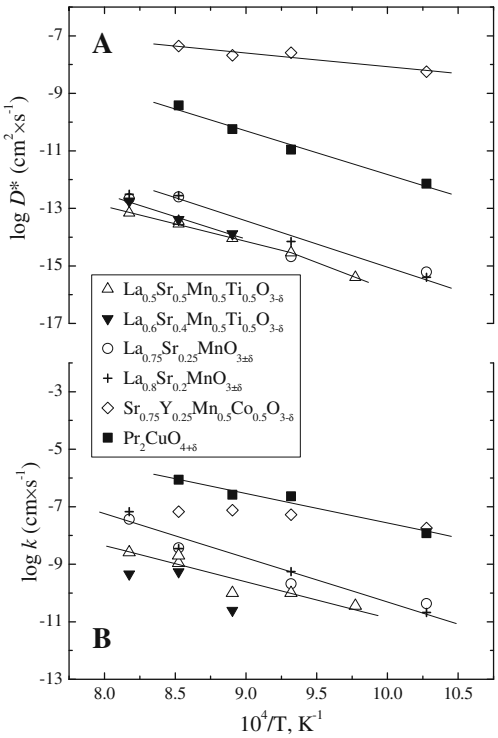

Fig. 16 Temperature dependencies of the bulk oxygen tracer diffusion (**a**) and surface exchange (**b**) coefficients of dense $La_{0.5}Sr_{0.5}Mn_{0.5}Ti_{0.5}O_{3-\delta}$ and $La_{0.6}Sr_{0.4}Mn_{0.5}Ti_{0.5}O_{3-\delta}$ ceramics compared to the data on lanthanum–strontium manganites, $Sr_{0.75}Y_{0.25}Mn_{0.5}Co_{0.5}O_{3-\delta}$ and $Pr_2CuO_{4+\delta}$ [15, 34] studied under identical conditions

$(La_{0.75-x}Sr_{0.25+x})_{0.95}Mn_{0.5}Cr_{0.5-x}Ti_xO_{3-\delta}$ system [7] where the contributions of both interfacial exchange and bulk ionic conduction are significant. While the behavior of the Cr-containing perovskites made it possible to detect a significant impact of the grain boundary diffusion, no similar conclusions can be drawn for the title system, although the grain boundary mechanism of ionic transport should not be a priori neglected. In particular, the steady-state permeation fluxes through dense $(La_{1-x}Sr_x)_{0.95}Mn_{0.5}Ti_{0.5}O_{3-\delta}$ membranes are, in fact, quite

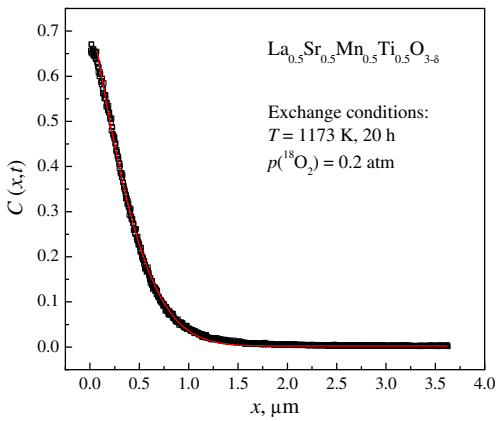

Fig. 17 Example of the ^{18}O penetration profile for $La_{0.5}Sr_{0.5}Mn_{0.5}Ti_{0.5}O_{3-\delta}$ at 1223 K. The *solid line* shows fitting results to the model Eq. 2

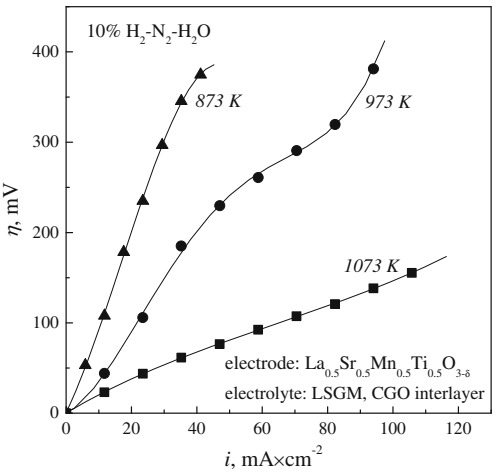

Fig. 18 Anodic overpotential vs. current density dependencies for porous $La_{0.5}Sr_{0.5}Mn_{0.5}Ti_{0.5}O_{3-\delta}$ electrode applied onto LSGM solid electrolyte with CGO interlayer, in humidified 10 % H_2–90 % N_2 flow at 873–1073 K

similar to one another due to very low oxygen nonstoichiometry (Fig. 14). In these conditions, the role of grain boundary diffusion is expected to increase as for lanthanum manganite [31, 32]. The low oxygen vacancy concentration is also responsible for relatively large scattering in the experimental data. Nevertheless, the oxygen permeability of $(La_{1-x}Sr_x)_{0.95}Mn_{0.5}Ti_{0.5}O_{3-\delta}$ tends to increase with increasing x in correlation with the oxygen nonstoichiometry variations revealed by the chemical expansion measurements. The permeation fluxes through $(La_{1-x}Sr_x)_{0.95}Mn_{0.5}Ti_{0.5}O_{3-\delta}$ ceramics are lower compared to $SrMnO_{3-\delta}$ based phases, such as $Sr_{0.7}Ce_{0.3}MnO_{3-\delta}$ [25], where the oxygen deficiency is substantially higher (Fig. 15). The apparent activation energies (Table 4) are high, typical for the perovskite compounds with almost stoichiometric oxygen sublattice when

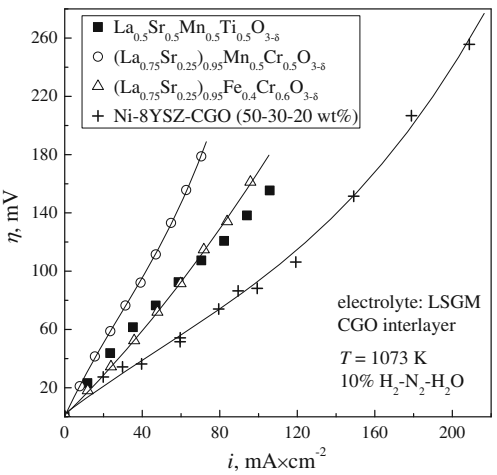

Fig. 19 Comparison of the anodic polarization curves of porous $La_{0.5}Sr_{0.5}Mn_{0.5}Ti_{0.5}O_{3-\delta}$ and other oxide [6, 38] and Ni-containing cermet [14] electrodes in contact with LSGM, collected under similar conditions in humidified 10 % H_2–90 % N_2 gas mixture at 1073 K

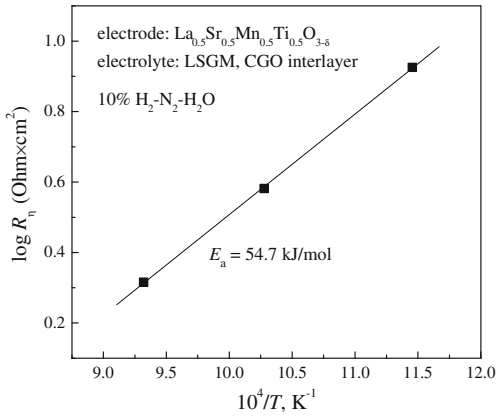

Fig. 20 Temperature dependence of the polarization resistance of porous $La_{0.5}Sr_{0.5}Mn_{0.5}Ti_{0.5}O_{3-\delta}$ anode applied onto LSGM with CGO interlayer, under open-circuit conditions

the E_a values comprise a large vacancy formation enthalpy contribution [33].

The results of the isotopic exchange experiments performed for A-site cation stoichiometric $La_{1-x}Sr_xMn_{0.5}Ti_{0.5}O_{3-\delta}$ are summarized in Fig. 16. Figure 17 displays one example of the depth profile collected for $La_{0.5}Sr_{0.5}Mn_{0.5}Ti_{0.5}O_{3-\delta}$ after exchanging with $^{18}O_2$ (0.2 atm) at 1173 K for 20 h, analyzed using Eq. 2. Note that the characteristic "tail" indicative of the grain boundary effect was visible, being more pronounced at lower temperatures; however, this phenomenon is still weaker than that in lanthanum–strontium manganites and was hence excluded from consideration in the present work. No attempt was performed to isolate this contribution to the isotopic diffusion by analogy with literature [18]. In agreement with the oxygen permeation data, the tracer diffusion coefficients in $La_{0.6}Sr_{0.4}Mn_{0.5}Ti_{0.5}O_{3-\delta}$ and $La_{0.5}Sr_{0.5}Mn_{0.5}Ti_{0.5}O_{3-\delta}$ are very

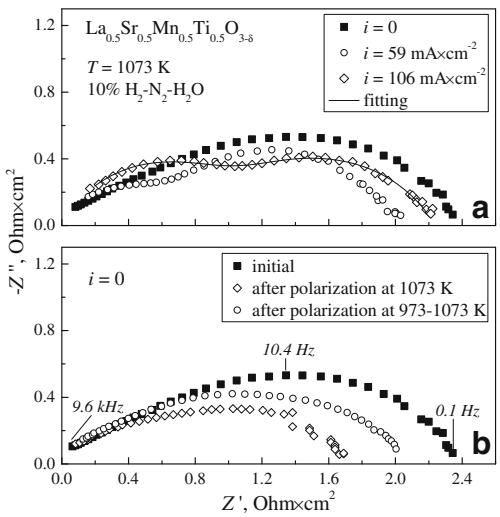

Fig. 21 Examples of typical impedance spectra corrected for the ohmic losses and normalized to the electrode surface area, measured at 1073 K and various DC densities (**a**) or under the open-circuit conditions before and after polarization (**b**)

similar to one another, whereas the surface exchange coefficients tend to increase with increasing x. The values of D^* are lower even with respect to lanthanum–strontium manganites, suggesting that the oxygen anions located near Ti^{4+} are essentially excluded from the migration processes. If compared to oxygen-deficient $Sr_{0.75}Y_{0.25}Mn_{0.5}Co_{0.5}O_{3-\delta}$ [34] and oxygen-hyperstoichiometric $Pr_2CuO_{4+\delta}$ [15], the difference in the oxygen diffusivity at atmospheric $p(O_2)$ is up to five to eight orders of magnitude. Regardless of the relevant microscopic mechanisms, this level of oxygen ionic transport is insufficient to expect any substantial enhancement of the electrochemical reaction zone due to diffusion in the electrode bulk as it has already been established for (La, Sr)MnO_3-based cathodes and (La, Sr) (Cr, Mn)O_3-based anodes (see [5, 6] and references cited therein).

Anodic performance

Summarizing the above discussion, one should stress that the chemical and thermal expansion of perovskite-type $(La_{1-x}Sr_x)_{1-y}Mn_{0.5}Ti_{0.5}O_{3-\delta}$ increases with increasing x (Figs. 6 and 7; Tables 2 and 3). The same trend was observed for electronic conduction in oxidizing atmospheres, whereas under reducing conditions the total conductivity values are essentially similar in the entire compositional range studied in this work (Figs. 8, 9, 10, and 11). The La-rich materials such as $(La_{0.85}Sr_{0.15})_{0.95}Mn_{0.5}Ti_{0.5}O_{3-\delta}$ exhibit smaller oxygen-nonstoichiometry variations on reduction and, thus, a more pronounced tendency to $p(O_2)$-independent concentration of the electronic charge carriers and conductivity at temperatures below 1100 K (Fig. 11c); however, their reduction is accompanied with apparently irreversible hysteresis phenomena (Fig. 12). Although the ionic transport parameters, including the oxygen permeability and surface exchange rate, tend to increase with x (Figs. 14 and 16), the overall level of ionic conduction is low; no significant influence on the electrode performance may be expected due to minor variations in the these parameters. Therefore, the compositions with intermediate strontium concentrations (x=0.4–0.6) seem to provide an optimum combination of the electronic transport and thermomechanical properties. In this compositional range, modest variations of the La/Sr concentration ratio and the creation of A-site cation deficiency have no significant impact on the total conductivity, especially under reducing conditions (Figs. 8, 9, and 10); the thermodynamic stability of the perovskite phases is also essentially unaffected by doping (Figs. 3 and 4). Consequently, for the assessment of anode performance, $La_{0.5}Sr_{0.5}Mn_{0.5}Ti_{0.5}O_{3-\delta}$ was selected as a model material.

Figures 18, 19, and 20 illustrate the behavior of porous $La_{0.5}Sr_{0.5}Mn_{0.5}Ti_{0.5}O_{3-\delta}$ electrode layers applied onto LSGM at 873–1073 K in H_2-containing atmosphere. Typical examples of the impedance spectra are shown in Fig. 21. At moderate current densities, the polarization resistance (R_η) is essentially

constant. However, anodic polarization has a non-negligible influence on the electrode impedance as for lanthanum–strontium manganite cathodes in oxidizing atmospheres [35–37]. As an example, after measuring the entire polarization curve with equilibration at each DC density and subsequent 2-h dwell under open-circuit conditions, the R_η derived from zero-bias impedance spectrum becomes approximately 30 % lower than the initial one (Fig. 21). After further operation during 45 h and temperature/current cycling, the polarization resistance slightly increased, indicating possible electrode degradation processes, although no microstructural alterations were detected by SEM. As for the $(La_{0.75-x}Sr_{0.25+x})_{0.95}Mn_{0.5}Cr_{0.5-x}Ti_xO_{3-\delta}$ electrodes [6, 7], the rate-determining steps should be related to the electrode surface; the key factors limiting anodic performance are expected to include the interfacial exchange kinetics and electronic conduction. One argument in favor of the non-negligible role of the electronic transport is that the activation energy for electrode conductivity (Fig. 20) is much lower than E_a values for oxygen permeability, diffusion, and surface exchange (Table 4; Fig. 16).

Whatever the electrode reaction mechanism, the electrochemical activity of $La_{0.5}Sr_{0.5}Mn_{0.5}Ti_{0.5}O_{3-\delta}$ anode layers appears significantly better than that of $(La_{0.75}Sr_{0.25})_{0.95}Mn_{0.5}Cr_{0.5}O_{3-\delta}$ [6] and is close to that of Mn-free $(La_{0.75}Sr_{0.25})_{0.95}Fe_{0.4}Cr_{0.6}O_{3-\delta}$ anodes [38] with similar microstructures (Fig. 19). Considering the negative effects associated with the presence of chromium in SOFCs, namely, volatilization of chromium oxides and formation of Cr^{6+}-containing phases in oxidizing conditions at low temperatures, $La_{0.5}Sr_{0.5}Mn_{0.5}Ti_{0.5}O_{3-\delta}$ and its analogs provide significant advantages with respect to the $LaCrO_3$-based electrode materials. The anodic overpotentials of $La_{0.5}Sr_{0.5}Mn_{0.5}Ti_{0.5}O_{3-\delta}$ are, however, still high in comparison with the Ni-containing cermets, thus making it necessary to incorporate the metallic and, possibly, catalytically active components in (La, Sr) (Mn, Ti)$O_{3-\delta}$ based anodes.

Acknowledgements This work was supported by the Ministry of Education and Science of the Russian Federation (state contract 02.740.11.5214) and by FCT—Portugal (projects SFRH/BPD/28629/2006 and SFRH/BD/45227/2008).

References

1. Fu QX, Tietz F (2008) Fuel Cells 08:283
2. Gong M, Liu X, Trembly J, Johnson C (2007) J Power Sources 168:289
3. Sun C, Stimming U (2007) J Power Sources 171:247
4. Tsipis EV, Kharton VV (2011) J Solid State Electrochem 15:1007
5. Tsipis EV, Kharton VV (2008) J Solid State Electrochem 12:1367
6. Kharton VV, Tsipis EV, Marozau IP, Viskup AP, Frade JR, Irvine JTS (2007) Solid State Ion 178:101
7. Kolotygin VA, Tsipis EV, Shaula AL, Naumovich EN, Frade JR, Bredikhin SI, Kharton VV (2011) J Solid State Electrochem 15:313
8. Fu QX, Tietz F, Stöver D (2006) J Electrochem Soc 153:D74
9. Ovalle A, Ruiz-Morales JC, Canales-Vázquez J, Marrero-López D, Irvine JTS (2006) Solid State Ion 177:1997
10. Kim JH, Miller D, Schlegl H, McGrouther D, Irvine JTS (2011) Chem Mater 23:3841
11. Escudero MJ, Irvine JTS, Daza L (2009) J Power Sources 192:43
12. Kharton VV, Shaula AL, Vyshatko NP, Marques FMB (2003) Electrochim Acta 48:1817
13. Bredikhin IS, Napol'skii FS, Korovkin EV, Istomin SY, Antipov EV, Bredikhin SI (2009) Russ J Electrochem 45:434
14. Tsipis EV, Kharton VV, Bashmakov IA, Naumovich EN, Frade JR (2004) J Solid State Electrochem 8:674
15. Kaluzhskikh MS, Kazakov SM, Mazo GN, Istomin SYa, Antipov EV, Gippius AA, Fedotov Yu, Bredikhin SI, Liu Yi, Svensson G, Shen Z (2011) J Solid StateChem 184:698
16. Crank J (1975) The mathematics of diffusion, 2nd edn. Oxford University Press, Oxford
17. Kilner JA, De Souza RA, Fullarton IC (1996) Solid State Ion 86–88:703
18. De Souza RA, Kilner JA, Walker JF (2000) Mater Lett 43:43
19. Shannon RD (1976) Acta Cryst A 32:751
20. Harwood MC (1955) Proc Phys Soc B 68:586
21. West AR (1984) Solid state chemistry and its applications. Wiley, Chichester
22. Tsipis EV, Kharton VV (2008) J Solid State Electrochem 12:1039
23. Mizusaki J (1992) Solid State Ion 52:79
24. Goodenough JB, Zhou JS (2001) Transport properties. In: Goodenough JB (ed) Localized to itinerant electronic transition in perovskite oxides. Springer, Berlin, pp 17–113
25. Marozau IP, Kharton VV, Viskup AP, Frade JR, Samakhval VV (2006) J Eur Ceram Soc 26:1371
26. Cumming DJ, Kharton VV, Yaremchenko AA, Kovalevsky AV, Kilner JA (2011) J Am Ceram Soc 94:2993
27. Hammami R, Harrouch Batis N, Batis H, Minot C (2009) Solid State Sci 11:885
28. Backhaus-Ricoult M (2006) Solid State Ion 177:2195
29. Zuev AYu, Tsvetkov DS (2010) Solid State Ion 181:557
30. Kharton VV, Nikolaev AV, Naumovich EN, Vecher AA (1995) Solid State Ion 81:201
31. Berenov AV, MacManus-Driscoll JL, Kilner JA (1999) Solid State Ion 122:41
32. Kharton VV, Marques FMB (2002) Curr Opin Solid State Mater Sci 6:261
33. Goodenough JB (2003) Ann Rev Mater Res 33:91
34. Burmistrov I, Drozhzhin OA, Istomin SY, Sinitsyn VV, Antipov EV, Bredikhin SI (2009) J Electrochem Soc 156:B1212
35. Lee HY, Cho WS, Oh SM, Wiemhöfer H-D, Göpel W (1995) J Electrochem Soc 142:2659
36. Jiang SP (2007) J Solid State Electrochem 11:93
37. Haider MA, McIntosh S (2009) J Electrochem Soc 156:B1369
38. Lü MF, Tsipis EV, Waerenborgh JC, Yaremchenko AA, Kolotygin VA, Bredikhin S, Kharton VV (2012) J Power Sources 206:59